# Concentrations of eBC from traffic and non-traffic sources

## DELIVERABLE 1.10

| | |
|---|---|
| **Author(s):** | Stephen Platt, Sabine Eckhardt |
| **Date of report:** | 08-12-2023 |
| **Version:** | 1 |
| **Responsible Partner:** | NILU |
| **Deliverable due Date:** | 30-09-2023 |
| **Dissemination Level:** | Public |

| | |
|---|---|
| **Call:** | HORIZON-CL5-2022-D1-02 |
| **Topic:** | Climate Sciences and Responses |
| **Project Type:** | Research and Innovation Action |
| **Lead Beneficiary:** | NILU - Norsk Institutt for Luftforskning |

## Document History

| Version | Date | Comment | Modifications made by |
|---|---|---|---|
| 0.1 | 12-12-2023 | First draft | Stephen Platt (NILU) |
| 0.2 | 13-12-2023 | Internal review | Hartmut Boesch |
| 1.0 | 19-12-2023 | Submitted to Commission following internal review | Stephen Platt (NILU) |

## Summary

Here we provide background information on the black carbon (BC) measurements within EYE-CLIMA, and methodological developments and results in the scope of Deliverable 1.10 of the EYE-CLIMA project: Concentrations of equivalent black carbon (eBC) from traffic and non-traffic sources.

# TABLE OF CONTENTS

# 1. Introduction

Aerosol particles including black carbon (BC) affect climate (Ramanathan and Carmichael 2008) and damage health (Dockery, Pope et al. 1993). The net climate effect of the atmospheric aerosol is a negative forcing (cooling), directly via scattering or indirectly via their influence on cloud formation (**Error! Reference source not found.**). However, for the strongly light absorbing fraction of the atmospheric aerosol such as black carbon, BC, or 'soot', the net climate effect is positive (warming), via radiative heating (Jacobson 2002) and changes in surface albedo resulting from deposition, particularly on snow or ice (Hadley and Kirchstetter 2012). Current uncertainties in BC forcing since the year 1750, representing the end of pre-industrial era, are larger than the estimated magnitude of the effect itself (**Error! Reference source not found.**).
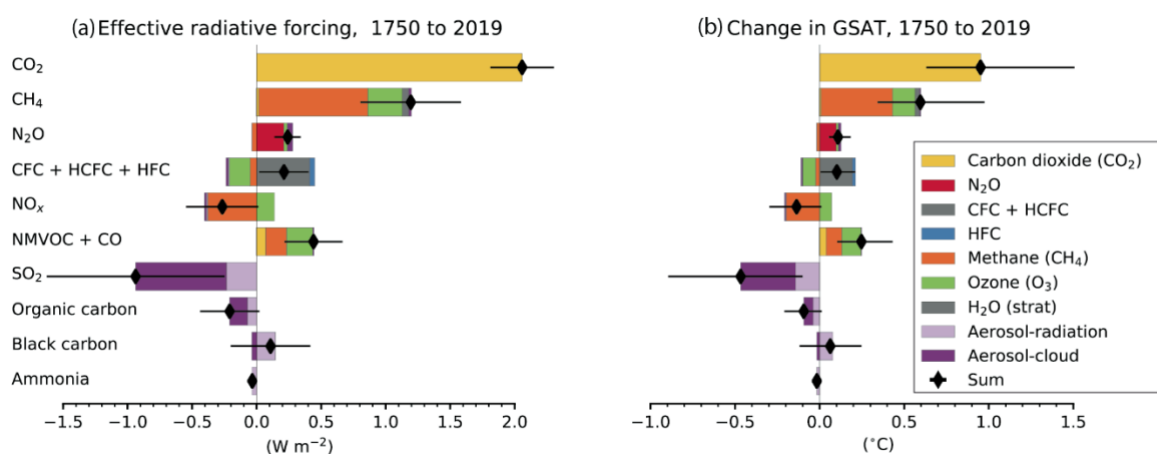


*Figure 1: The change in effective radiative forcing (a) and global surface average temperature (GSAT, b) between 1750 and 2019 due to changes in the listed atmospheric components (carbon dioxide, $CO_2$; methane, $CH_4$; nitrous oxide, $N_2O$; chlorofluorocarbons, CFC+ hydro chlorofluorocarbons, HCFC+ hydrofluorocarbons HFC; oxides of nitrogen, $NO_X$; non-methane volatile organic compounds, NMVOC, sulfate aerosol $SO_2$, organic carbon, black carbon, ammonia), according to the IPCC AR6, 2021 (Masson-Delmotte, Zhai et al. 2021).*

This uncertainty in BC climate forcing arises due to the difficulty in accurately modeling the atmospheric processing of BC and due to uncertainties in emissions (Lee, Reddington et al. 2016). Uncertainties in emissions arise due to lack of knowledge of source strengths from various sectors, including fossil fuel combustion and particularly residential heating, but also due to the operational nature of the definition of BC and the influence this has on model-observation comparisons (Vignati, Karl et al. 2010).

Two techniques for quantifying BC are thermal optical analysis and light extinction methods. In thermal optical analysis the volatile aerosol is removed via heating and the remaining, graphite-like, elemental carbon (EC) is quantified. A widely used extinction method is to measure the attenuation (ATN) of light across a filter material with photo-absorption spectrometers such as the 'aethalometer':

$$ATN = -100 \times \frac{I}{I_0} \quad , \qquad (1)$$

where $I$ is the measured light intensity through the filter spot and $I_0$ the reference intensity. This is used to determine an absorption coefficient ($B_{Abs}$) relating the change in measured attenuation $\Delta ATN$ to optical thickness in ambient air:

$$B_{Abs} = \frac{s \times (\Delta ATN/100)}{F(1 - \zeta) \times C \times (1 - k \times ATN) \times \Delta t} \quad , \qquad (2)$$

where $F$ is the flow rate, $k$ is the loading compensation parameter, $\Delta t$ is the time step, and the constants $s$, $\zeta$, and $C$ are the spot size, lateral flow above the filter and the multiple scattering correction factor, respectively (Drinovec, Močnik et al. 2015). Note that $C$ can have significant uncertainty when measuring highly scattering particles (i.e., high single scattering albedo, typically in large particles with diameter in the wavelength range of measurements, e.g., mineral dust) and is dependent on the filter material or tape type used (Yus-Díez, Bernardoni et al. 2021). In multiwavelength aethalometers, $B_{Abs}$ is measured at seven wavelengths ($\lambda$= 370; 470; 520; 590; 660; 880; 950 nm), and may be converted into an equivalent black carbon (eBC) concentration relating absorption to BC using a mass absorption cross-section (MAC):

$$eBC(\lambda) = B_{Abs}(\lambda)/MAC(\lambda) \tag{3}$$

Normally, eBC is determined at $\lambda$= 880 nm, and when possible, using co-located EC measurements:

$$MAC(\lambda) = B_{Abs}(\lambda)/EC. \tag{4}$$

In doing so, the parameters $s$, $\zeta$, and $C$ in (2) can be neglected. This is advantageous in case of uncertainty in e.g. $C$, which varies with filter material and in case of significant scattering affecting the extinction (a function of aerosol size and type, i.e. single scattering albedo). If $s$, $\zeta$, and $C$ are unconstrained EC is used as a de facto empirical conversion factor. Following this procedure, the MAC is unconstrained, i.e., (4) yields an *effective* MAC, MAC*.

Measuring multiple wavelengths yields information on the presence of incomplete combustion products within BC particles. The wavelength dependence of absorption can be expressed as a single parameter, the absorption Ångstrøm exponent (AAE), which describes the power law dependence of absorption on wavelength:

$$B_{Abs}(\lambda) = B_{Abs,0} \times \left(\frac{\lambda}{\lambda_0}\right)^{-AAE}, \tag{5}$$

where $\lambda_0$ is the reference wavelength, and $B_{Abs,0}$ the reference absorption coefficient. AAE time series can be determined from multiwavelength measurements from a single wavelength pair by re-arranging (5) or via linear regression of log $B_{Abs}$ vs log $\lambda$ where AAE is then the negative of the slope.

Theoretically, pure BC from complete combustion under lean conditions has an AAE of 1 (Kirchstetter, Novakov et al. 2004), though in ambient air some scattering effects can occur due to atmospheric processing or condensation of co-emitted species such as sulfur resulting in scattering, further reducing the AAE to <1 (Helin, Virkkula et al. 2021). The lean combustion conditions required to produce pure graphitic carbon rarely exist in nature and $B_{Abs}$ or eBC with AAE ~1 or lower is almost exclusively produced in internal combustion engines, or other lean combustion scenarios with liquid fuels, and mostly reflects fossil fuel combustion or traffic (though not exclusively). In general, higher AAE values, AAE >1, reveal the presence of light absorbing compounds formed during fuel-rich combustion (Saleh, Robinson et al. 2014). This is more likely to occur during solid fuel burning such as in residential heating using wood combustion, or wildfires. Using these assumptions, it is possible to estimate eBC from liquid and solid fuel sources, eBC$_{(l)}$, eBC$_{(s)}$, using the aethalometer model (Sandradewi, Prévôt et al. 2008, Zotter, Herich et al. 2017):

$$B_{Abs\,(s)}(\lambda_2) = \frac{B_{Abs}(\lambda_1) - B_{Abs}(\lambda_2) \times \left(\frac{\lambda_1}{\lambda_2}\right)^{-AAE_{(l)}}}{\left(\frac{\lambda_1}{\lambda_2}\right)^{-AAE_{(s)}} - \left(\frac{\lambda_1}{\lambda_2}\right)^{-AAE_{(l)}}}, \quad (6)$$

$$B_{Abs\,(l)}(\lambda_2) = \frac{B_{Abs}(\lambda_1) - B_{Abs}(\lambda_2) \times \left(\frac{\lambda_1}{\lambda_2}\right)^{-AAE_{(s)}}}{\left(\frac{\lambda_1}{\lambda_2}\right)^{-AAE_{(l)}} - \left(\frac{\lambda_1}{\lambda_2}\right)^{-AAE_{(s)}}}, \quad (7)$$

where $(\lambda_2)$ and $(\lambda_1)$ are a pair of higher and lower wavelengths at which measurements are made, respectively, and $AAE_{(l)}$ and $AAE_{(s)}$ are the a priori AAE for the liquid and solid fuel contributions to $B_{Abs}$. Equations (6) and (7) are a simple source apportionment method for B$_{Abs}$ and hence eBC after conversion via the MAC, assuming that the MAC is the same for both liquid and solid fuel contributions and that the data are represented only by two contributing factors. However, AAE is known to vary widely by source and widely in ambient air due to processing. Furthermore, since the factors have a power law dependence, uncertainty in AAE causes very high uncertainty in the resulting factors.

To constrain climate forcing due to BC within the scope of future modeling work of EYE-CLIMA, it is necessary to reduce uncertainties in emissions, particularly from traffic and residential wood burning sectors. Here we use a new application of non-negative matrix factorization (NNMF) to determine liquid and solid fuel contributions to eBC across Europe, which assuming these well represent BC from vehicles and residential heating, will be used to constrain BC from these sectors in inversion models and reduce uncertainty in the BC climate forcing. Further, by using EC measurements where available to determine MAC* we produce a harmonized, quality assured dataset of eBC and $B_{Abs}$ for Europe using a consistent methodological approach, which alongside the new NNMF script, will be publicly available for dissemination.

## 2. Methodology

### 2.1 Description of measurement locations

We obtained absorption coefficients from 7-wavelength aethalometer measurements (Magee, AE33) at 28 sites between 01.01.2015 and 31.12.2022 comprising a mix of urban, peri-urban, and regional and global background sites (Figure 2) with settings described in Table 1, mostly via the ebas data portal (ebas.nilu.no, 25 sites) or by correspondence (Oslo Sofienberg Park, Norway; Krakow, Poland; and University College Dublin, Ireland). Global sites represent locations far from local sources, e.g., the Zeppelin Observatory, and are regarded as measurement locations for atmospheric background levels of atmospheric constituents (Platt, Hov et al. 2022). They typically have the lowest levels of air pollutants, with elevated levels only during long range transport events. Regional settings are typically rural with atmospheric pollutants from the region, with frequent pollution events due to long range transport (Yttri, Canonaco et al. 2021), but generally lower levels than sites in the Urban category. Urban and peri-urban sites are located within or at the periphery of major settlements and experience significant influence of e.g., residential heating and traffic. The characteristics of the air pollutants are likely to be influenced by local factors such as topography, vehicle pollution regulations and traditional fuel use in the home (e.g., wood burners vs coal combustion etc.).

*Table 1:   Summary of sites, locations, and settings of the $B_{abs}$ observation data collected and harmonized in EYE-CLIMA*

| Station code | Station name | Country | Station setting | Latitude [degrees] | Longitude [degrees] | Measurement Altitude [m] |
|---|---|---|---|---|---|---|
| CH0001G | Jungfraujoch | Switzerland | Global | 46.548 | 7.985 | 3578 |
| CH0002R | Payerne | Switzerland | Regional | 46.813 | 6.945 | 493 |
| CH0005R | Rigi | Switzerland | Regional | 47.068 | 8.463 | 1035 |
| CH0010U | Zürich-Kaserne | Switzerland | Urban | 47.378 | 8.530 | 412 |
| CY0002R | Agia Marina Xyliatou | Cyprus | Regional | 35.039 | 33.058 | 532 |
| DE0043G | Hohenpeissenberg Observatory | Germany | Global | 47.800 | 11.020 | 975 |
| ES0019U | Barcelona | Spain | Urban | 41.390 | 2.116 | 80 |
| ES0020U | Granada | Spain | Urban | 37.164 | -3.605 | 680 |
| ES0021U | Madrid | Spain | Urban | 40.456 | -3.723 | 673 |
| FI0096G | Pallas (Sammaltunturi) | Finland | Global | 68.00 | 24.15 | 572 |
| FR0020R | SIRTA Atmospheric Research Observatory | France | Regional | 48.709 | 2.158 | 177 |
| FR0027U | Villeneuve d'Ascq | France | Regional | 50.611 | 3.140 | 90 |
| FR0035U | Marseille-Longchamp | France | Urban | 43.305 | 5.395 | 64 |
| GB0101U | Birmingham Air Quality Site | UK | Urban | 52.456 | -1.929 | 146 |
| GR0100B | Athens Demokritas | Greece | Urban background | 37.995 | 23.816 | 280 |
| IE0010U | University College Dublin | Ireland | Urban | 53.309 | 6.225 | 35 |
| IT0025U | Milano Pascal | Italy | Urban | 45.478 | 9.231 | 121.5 |
| IT0026U | Rome (Villa Ada) | Italy | Urban | 41.933 | 12.507 | 64 |
| IT0027U | Milano Marche | Italy | Urban | 45.465 | 9.189 | 131.5 |
| IT0028U | Milano Senato | Italy | Urban | 45.470 | 9.197 | 123.5 |
| NO0002R | Birkenes Observatory | Norway | Regional | 58.389 | 8.252 | 219 |
| NO0042G | Zeppelin Observatory | Norway | Global | 78.907 | 11.888 | 475 |
| NO0073U | Oslo - Sofienbergparken | Norway | Urban background | 59.967 | 10.756 | 27.4 |
| PL0010U | Krakow | Poland | Urban | | | 232 |
| RO0007R | Bucharest | Romania | Regional, peri-urban | 44.348 | 26.029 | 170 |
| SE0021R | Hyltemossa | Sweden | Regional | 56.098 | 13.419 | 145 |
| SE0024U | Stockholm (Hornsgatan 108) | Sweden | Urban | 59.317 | 18.048 | 46 |
| SE0025U | Stockholm (Torkel Knutssonsgatan) | Sweden | Urban | 59.316 | 18.058 | 62 |
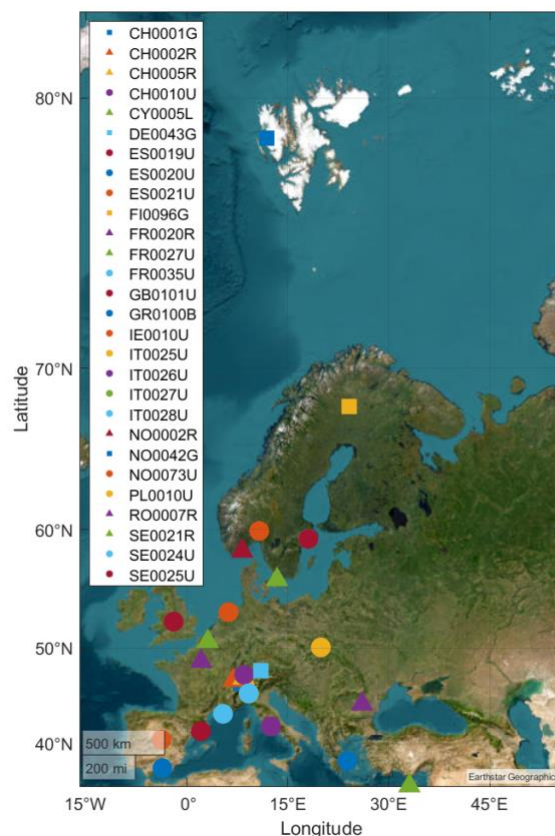
*Figure 2: Measurement locations of aethalometer data in EYE-CLIMA. Global sites are represented by squares, regional sites by circles, and other station settings by triangles.*

## 2.2 Data harmonization and quality control

After we downloaded aethalometer data from ebas (ebas.nilu.no), we performed an initial quality control step by checking consistency of the absorption coefficients with regard to column header and order, e.g. ensuring that data was in the correct order in the file with respect to stated measurement wavelength or did not represent measurement uncertainty rather than actual data (in the ebas Nasa AMES format, the raw data from the instrument is averaged to 1 hour and recorded alongside the uncertainty is calculated based on variation within that hour). We then re-gridded all data to a harmonized time step of 1 hour intervals between 01.01.2015 and 31.12.2022. No data series was 100% complete within this interval and the resulting, re-gridded, time series contained empty entries (NaNs, 'not a number').

As an additional quality control measure, and to remove outliers in a consistent way, we determined the $R^2$ from fits of log $B_{Abs}$ vs log wavelength, replacing every hour of data with $R^2 < 0.99$ with NaN, a procedure also adopted by (Tobler, Skiba et al. 2021). Note that the log $B_{Abs}$ vs log wavelength fits typically have very high $R^2$, such that $R^2 = 0.99$ is below the 99th percentile. For the global sites, this step did result in replacing a significant number of points, e.g., around half for CH0001G (Jungfraujoch). It is important to note, however, that such data are derived from low values which are considered as below instrument detection limits as defined in the downloaded files.

Lastly, data were converted to standard temperature and pressure (273.15 K, 100 kPa). We did this for consistency since in the files for many sites it is either stated that data are at this temperature and pressure, without further information on ambient conditions, or the measurements are in ambient conditions with information on the conditions given. Accordingly, the only possible step for

9

harmonization is conversion of data given in ambient temperature and pressure to standard conditions. Note that according to the ideal gas law, a variation in temperature by 20 K, easily observed at most sites, will result in a 7% difference in $B_{Abs}$, not including the effect of pressure.

## 2.3 Source apportionment

The aim of this work was to apportion BC to residential wood burning and traffic. For most sites this is approximated by high and low AAE values in the aethalometer data, or AAE values representative of solid fuel and liquid fuel, respectively. As a first step (from here on in 'Model 1', M1) we used Equations 6 and 7 (See section 1) for the apportionment. We used an AAE(l)=1 and AAE(s)=2, following (Sandradewi, Prévôt et al. 2008).

Since it is difficult to accurately determine AAE pairs for all sites and given the exponential effect of the uncertainties in AAEs in Equations 6 and 7, this apportionment frequently results in apparent negative $B_{Abs}$ in the resulting time series, also seen in data in e.g., (Zotter, Herich et al. 2017). To avoid the need for a priori knowledge of the AAEs we implemented a new application of the non-negative matrix factorisation approach first developed by (Lee and Seung 2000). This approach assumes that a bulk data matrix V of i rows and j columns (here $V = B_{Abs}$, i= time, j=λ) is approximated by the sum of non-negative factors of number or rank R (here R=2, i.e., liquid fuel and solid fuel):

$$V_{i,j} \approx (WH)_{i,j} = \sum_{a=1}^{R} W_{i,a} H_{a,j} , \qquad (8)$$

where W is the factor time series matrix and H a weight coefficient or 'factor profile' matrix

The NNMF approach then proceeds as follows:

(1) Initial generation of random non-negative matrices $W^{n=0}$, $H^{n=0}$, (random seed)
(2) Apply the following update rules by increasing step *n* by +1:

$$H^{n+1} = H^n \times \left( \frac{(W^n)^T V}{(W^n)^T W^n H^n} \right), \qquad (9)$$

$$W^{n+1} = W^n \times \left( \frac{V(H^{n+1})^T}{W^n H^{n+1} (H^{n+1})^T} \right), \qquad (10)$$

(3) Impose non-negative values constraint by replacing negative values with a very low value, $10^{-10}$.
(4) Repeat steps 2 and 3 until a stopping criterion is met, here defined as a difference in the relative fractions of W between steps n of <0.0001.
(5) Sort the factors. Note that the order of the resulting time series in the NNMF output is random. However, AAEs may be effectively determined from the factor profiles via a fit of log $H_{a,j}$ vs log $λ_j$. Hence to sort or 'map' the resulting matrices we determined the effective AAEs and sorted the factor positions from low to high. Given that liquid fuel has lower AAE than solid fuel we assume factor 1= liquid fuel $B_{Abs}$ ≈traffic related $B_{Abs}$ and factor 2 = solid fuel $B_{Abs}$ ≈wood burning $B_{Abs}$.
(6) Finally, we performed 100 repeats of the NNMF routine (1 to 5) and calculated the final factor profiles and time series from the averaged result.

In Equation 9 the coefficient matrix $H^n$ is updated by minimizing the difference in the resulting time series compared to the bulk matrix V. This updated coefficient matrix $H^{n+1}$ is used in Equation 10 to minimize the feature matrix (factor time series) W compared to V. We wrote the analysis script and performed the analysis in the proprietary software package Igor Pro (Wavemetrics) and produced a

Python script of the algorithm for dissemination. To convert the factors into eBC we used collocated EC measurements and $B_{Abs}$ at λ=880 nm with Equation 4 where possible. If co-located EC measurements were not available, we used the default instrument setting $MAC_{880nm}$=7.77 $m^2$ $g^{-1}$.

We used the factor-derived effective AAEs in the Equations in the aethalometer model (Equations 6 and 7) in a second, hybrid, source apportionment model (M2). The time series W also directly represents time series of liquid fuel or traffic and solid fuel or wood burning BC purely derived via NNMF, from hereon in referred to as model 3 (M3).

## 3. Results

Previously, (Tobler, Skiba et al. 2021) used the probability distribution of the AAE values as a function of time in the bulk absorption data to manually identify suitable AAE values for use in the aethalometer model, with the basic assumption being that the lowest and highest AAEs are observed at the minimum and maximum relative contributions from the liquid fuel source, respectively. Hence these values should approximately represent the AAEs of the pure sources. Here we observe that the NNMF algorithm also yields factors with AAE values close to the edges of the distribution, suggesting that NNMF yields factor profiles representative of the AAEs of the pure sources (Figure 3), with the advantage that manual selection of the most representative parts of the distribution best representing the AAE of the pure source is not required.
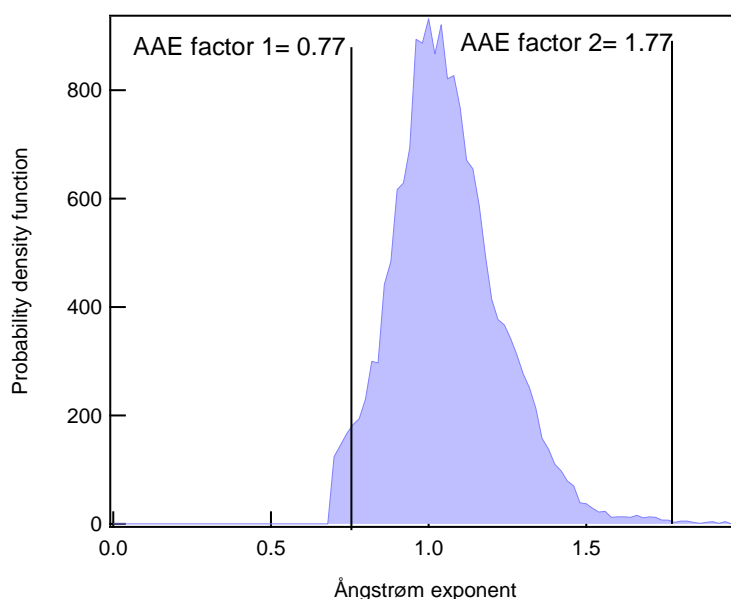


*Figure 3: Probability distribution of absorption Ångstrøm exponents in the absorption data over time at the Zeppelin Observatory (blue shaded area) and the factor derived AAE values, black lines.*

Note, the exact AAE is still somewhat uncertain in the approach of (Tobler, Skiba et al. 2021), due to its likely variability in time and accounting for measurement uncertainties. Hence it is still unclear which parts of the distribution of AAEs in the bulk data are most representative.

In Figure 4 we compare the solid fuel fractions obtained at all sites in M2 and M3. We observe a very high correlation between the approaches, $R^2$=0.93, suggesting that NNMF M2 and M3 closely approximate M1 when representative AAEs are selected from the AAE distribution (Figure 3), though with the advantage of avoiding manually selecting AAEs from the distribution and avoiding negative values due to the non-negativity constraint of the NNMF algorithm.
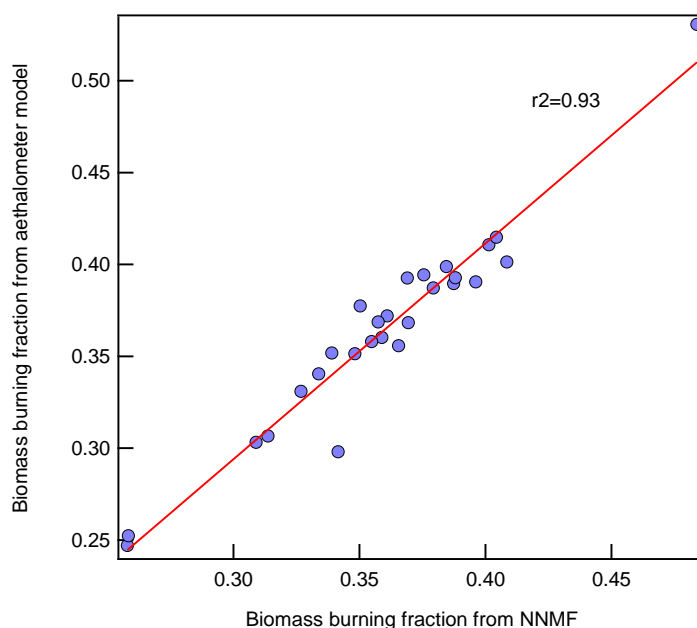
*Figure 4: Relative fraction of factor 2 (biomass burning) from the aethalometer model using NNMF derived AAEs (model 2, see main text) vs the relative fraction according to purely NNMF derived time series (Model 3, see main text) for all measurement sites.*

Yttri, Canonaco et al. (2021), and Yttri, Bäcklund et al. (2023) also determined liquid and solid fuel source contributions by NNMF using the positive matrix factorization (PMF) algorithm. The main advantage of the multiplicative update routine (e.g., Equations 9 and 10) vs PMF is that it is computationally less expensive, i.e., faster, and does not require a matrix of measurement uncertainties (not available in the level 2 data in ebas). We compared the two approaches on data from the Zeppelin observatory used in Yttri, Bäcklund et al. 2023, observing close agreement, e.g., PMF found a biomass burning contribution of 27 to 32 % vs a slightly lower 23% according to NNMF.

All three source apportionment models estimate higher biomass burning contributions in winter vs summer (Figure 5) with M3 predicting lower contributions compared to the other models. The highest concentrations of eBC are observed in winter at Northern and Eastern European sites and in Italy. In summer, high concentrations are seen in southern Europe, which may be linked to wildfires.
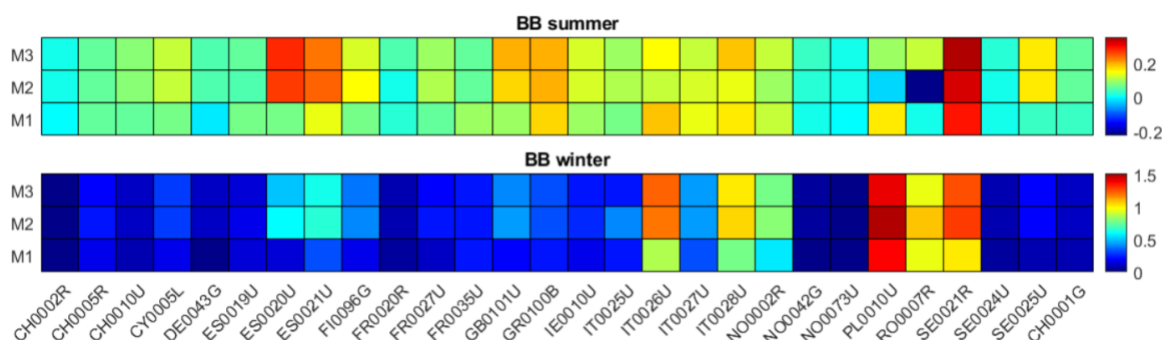


*Figure 5: Concentrations of solid fuel sources of equivalent black carbon (eBC, likely mostly biomass burning, BB) during summer and winter at the 28 sites for eBC analysis in EYE-CLIMA. Results are shown for the three source apportionment models in this study, Model 1 (M1): the aethalometer model, see equation 6 an 7, main text, using absorption Ångström exponents (AAEs) of 1 and 2 for liquid and solid fuels, respectively; M2: a hybrid model using NNMF output derived AAEs in the aethalometer model, and M3: the concentrations of eBC according to the NNMF output time series. Concentrations are indicated by the colour scale, the sites labeled on the x-axis are presented in Table 1.*

The diurnal pattern of solid fuel eBC fraction for winter (December, January, February) is shown in Figure 6. All sites show elevated contributions for wood burning in the evening and first part of the day. Interestingly, the highest relative contribution of solid fuel eBC is at the regional sites with overall low concentrations in Figure 5. This suggests that eBC in the wider European region is dominated by residential heating emissions in winter.
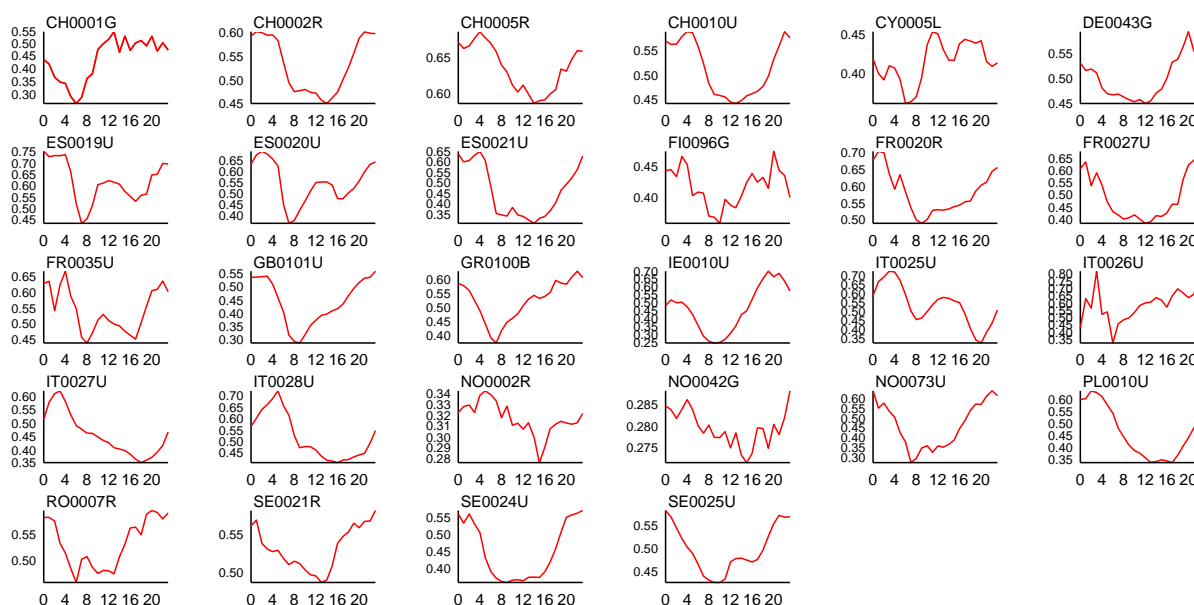


*Figure 6: Diurnal variation of the relative contribution of solid fuel eBC to total eBC at the 28 EYE-CLIMA sites in winter.*

*Table 1: Output parameters and filenames made publicly available in EYE-CLIMA deliverable 1.10. The index 'p' denotes the time dimension, q for the site dimension.*

| Parameter and dimension [] | Filename | Note |
|---|---|---|
| Station code [q] | StationList_v2.csv | These are the emep names including class |
| Time stamp [p] | TimeStamp.csv | All data have the same time dimension |
| Model 1 liquid fuel [p][q] | TS_FF_M1.csv | Use TS_FF_M1[p][q]*Mac[q] for Babs |
| Model 2 liquid fuel [p][q] | TS_FF_M2.csv | |
| Model 3 liquid fuel [p][q] | TS_FF_M3.csv | |
| Model 1 Solid fuel [p][q] | TS_BB_M1.csv | |
| Model 2 Solid fuel [p][q] | TS_BB_M2.csv | |
| Model 3 solid fuel [p][q] | TS_BB_M3.csv | |
| MAC values [q] | MAC.csv | |
| eBC880[p][q] | TS_880.csv | |
| Station latitude [q] | Latitude_v2.csv | Decimal |
| Station longitude [q] | Longitude_v2.csv | Decimal |
| Measurement altitude [q] | Altitude_v2.csv | Meters above sea level |

The output data of all three apportionment models, station parameters and other physical parameters will be made available to the public according to the data policy of EYE-CLIMA (https://eyeclima.eu/products/public-reports/). Here we will store the data in data arrays e.g., in a machine-readable format with documentation for meta data. The data from Deliverable 1.10 are also available on request, e.g., via the EYE-CLIMA webpage at https://eyeclima.eu/contact/.

## 4. Conclusions and outlook

In EYE-CLIMA deliverable 1.10 we have provided large scale intercomparisons of source apportioned eBC in Europe using data treated in a harmonized way and the first to include an alternative methodology not requiring a priori knowledge of AAEs, thereby avoiding large uncertainties and negative concentrations in the output time series. As such this data will be useful for creating improved emissions estimates via inversion methodologies e.g. FLEXINVERT (Thompson and Stohl 2014) and as part of EYE-CLIMA, as previously applied to BC times series (though not source-apportioned) in for example (Evangeliou, Platt et al. 2021). This will be useful to reduce the uncertainties in estimates of radiative forcing due to BC as shown in  Figure 1. Future work might focus on validation of the source apportionment work, for example via comparison to levoglucosan.

## 5. References

Dockery, D. W., et al. (1993). "An association between air pollution and mortality in six US cities." New England journal of medicine 329(24): 1753-1759.

Drinovec, L., et al. (2015). "The" dual-spot" Aethalometer: an improved measurement of aerosol black carbon with real-time loading compensation." Atmospheric Measurement Techniques 8(5): 1965-1979.

Evangeliou, N., et al. (2021). "Changes in black carbon emissions over Europe due to COVID-19 lockdowns." Atmospheric Chemistry and Physics 21(4): 2675-2692.

Hadley, O. L. and T. W. Kirchstetter (2012). "Black-carbon reduction of snow albedo." Nature Climate Change 2(6): 437-440.

Helin, A., et al. (2021). "Variation of absorption Ångström exponent in aerosols from different emission sources." Journal of Geophysical Research: Atmospheres 126(10): e2020JD034094.

Jacobson, M. Z. (2002). "Control of fossil-fuel particulate black carbon and organic matter, possibly the most effective method of slowing global warming." Journal of Geophysical Research: Atmospheres 107(D19): ACH 16-11-ACH 16-22.

Kirchstetter, T. W., et al. (2004). "Evidence that the spectral dependence of light absorption by aerosols is affected by organic carbon." Journal of Geophysical Research: Atmospheres 109(D21).

Lee, D. and H. S. Seung (2000). "Algorithms for non-negative matrix factorization." Advances in neural information processing systems 13.

Lee, L. A., et al. (2016). "On the relationship between aerosol model uncertainty and radiative forcing uncertainty." Proceedings of the National Academy of Sciences 113(21): 5820-5827.

Masson-Delmotte, V., et al. (2021). "Ipcc, 2021: Summary for policymakers. in: Climate change 2021: The physical science basis. contribution of working group i to the sixth assessment report of the intergovernmental panel on climate change."

Platt, S. M., et al. (2022). "Atmospheric composition in the European Arctic and 30 years of the Zeppelin Observatory, Ny-Ålesund." Atmospheric Chemistry and Physics 22(5): 3321-3369.

Ramanathan, V. and G. Carmichael (2008). "Global and regional climate changes due to black carbon." Nature geoscience 1(4): 221-227.

Saleh, R., et al. (2014). "Brownness of organics in aerosols from biomass burning linked to their black carbon content." Nature geoscience 7(9): 647-650.Sandradewi, J., et al. (2008). "Using aerosol light absorption measurements for the quantitative determination of wood burning and traffic emission contributions to particulate matter." Environmental science & technology 42(9): 3316-3323.

Thompson, R. L. and A. Stohl (2014). "FLEXINVERT: an atmospheric Bayesian inversion framework for determining surface fluxes of trace species using an optimized grid." Geoscientific Model Development 7(5): 2223-2242.

Tobler, A. K., et al. (2021). "Characterization of non-refractory (NR) PM 1 and source apportionment of organic aerosol in Kraków, Poland." Atmospheric Chemistry and Physics 21(19): 14893-14906.

Vignati, E., et al. (2010). "Sources of uncertainties in modelling black carbon at the global scale." Atmospheric Chemistry and Physics 10(6): 2595-2611.

Yttri, K. E., et al. (2023). "Composition and sources of carbonaceous aerosol in the European Arctic at Zeppelin Observatory, Svalbard." EGUsphere 2023: 1-49.

Yttri, K. E., et al. (2021). "Trends, composition, and sources of carbonaceous aerosol at the Birkenes Observatory, northern Europe, 2001–2018." Atmospheric Chemistry and Physics 21(9): 7149-7170.

Yus-Díez, J., et al. (2021). "Determination of the multiple-scattering correction factor and its cross-sensitivity to scattering and wavelength dependence for different AE33 Aethalometer filter tapes: A multi-instrumental approach." Atmospheric Measurement Techniques 14(10): 6335-6355.

Zotter, P., et al. (2017). "Evaluation of the absorption Ångström exponents for traffic and wood burning in the Aethalometer-based source apportionment using radiocarbon measurements of ambient aerosol." Atmospheric Chemistry and Physics 17(6): 4229-4249.

https://eyeclima.eu